Positive cerium anomalies imply pre-GOE redox stratification and manganese oxidation in Paleoproterozoic shallow marine environments

Matthew R. Warke[1,2], Harald Strauss[3] and Stefan Schröder[1]

[1]Basin Studies and Petroleum Geoscience, School of Earth and Environmental Sciences, University of Manchester, Manchester M13 9PL, United Kingdom

[2]School of Earth and Environmental Sciences, University of St Andrews, St Andrews, KY16 9AL, United Kingdom; mw438@st-andrews.ac.uk

[3]Geologisch-Paläontologisches Institut der Westfälischen Wilhelms-Universität Münster, Correnstraße 24, 48149, Münster, Germany

The Paleoproterozoic Koegas Subgroup (Transvaal Supergroup, South Africa) was deposited in the immediate prelude to the Great Oxidation Event (GOE), and can therefore shed light on the oceanic paleoredox conditions just before atmospheric oxidation. Manganese enrichments of ~16 wt% in diagenetic kutnahorite horizons suggest that Mn^{2+} oxidation occurred, either by free O_2 or by an ancient photosystem. Iron and molybdenum isotope trends also support the existence of a Mn^{4+}-oxide sediment flux, suggesting that the Koegas basin may have been redox stratified. Evidence from detrital and authigenic pyrite with mass-independently fractionated sulfur isotopes, however, suggests that the atmosphere was devoid of oxygen. To resolve this contradiction, this paper presents new constraints on pathways of Mn^{2+} oxidation from field, petrographic, stable isotope, and rare earth element and yttrium (REY_{SN}) analysis of stromatolitic carbonates from the upper Koegas Subgroup. Ferroan dolostones and limestones preserve marine REY_{SN} arrays with positive Ce_{SN} anomalies. These differences are explained by a redox stratified basin, whereby Mn^{2+} and Ce^{3+} are oxidized at a redoxcline and Ce is adsorped onto sinking Mn-oxide particles. Mn-oxide particles and a negative Ce anomaly from the oxidized upper water column are transferred into carbonates accumulating above the redoxcline. Diagenetic fluids later reduce the Mn-oxides to kutnahorite. Below the redoxcline, reduction of Mn-oxides particles enriches carbonates in Mn and a positive Ce anomaly. This contribution adds evidence for development of oxygen oases and redox-stratified basins before the GOE. Redox stratification was best developed during transgressions. During regressions, a deltaic system prograded into the Koegas Basin. High sedimentation rates likely allowed for preservation of detrital pyrite only in the deltaic sandstones, thus explaining the contradictory geochemical evidence. No previously unknown ancient photosystem of Mn oxidation is required to explain Mn oxidation.

Keywords: Koegas; Transvaal; Great Oxidation Event; Rare Earth Elements; Cerium

1. Introduction

Late Neoarchean to early Paleoproterozoic authigenic sediments deposited on the Kaapvaal Craton record evidence for trace levels of free oxygen (O_2) in surface waters, and possibly in the atmosphere, for at least transient periods (Wille et al., 2007; Garvin et al., 2009; Godfrey and Falkowski, 2009; Voegelin et al., 2010). In the Griqualand West Basin paleoredox studies of the Neoarchean Campbellrand Subgroup (Figure 1), employing nitrogen isotopes (Garvin et al., 2009; Godfrey and Falkowski, 2009), molybdenum isotopes (Wille et al., 2007; Voegelin et al., 2010), coupled molybdenum and iron isotopes (Czaja et al., 2012) and coupled molybdenum and rhenium concentrations (Kendall et al., 2010), suggest that trace O_2 was being produced in shallow marine settings, albeit in levels too low to permit cerium oxidation and preserve cerium anomalies (Eroglu et al., 2017; Warke et al., 2019). However, the persistence of mass-independently fractionated sulfur isotopes (S-MIF) in Campbellrand Subgroup shales implies the Neoarchean atmosphere remained reducing (Izon et al, 2015; 2017; Zerkle et al., 2012). Complete S-MIF disappearance, marking the onset of atmospheric oxygenation and the establishment of a stable ozone layer, is only recorded 100-200 Myr later, in the laterally correlative Paleoproterozoic Duitschland and Rooihoogte formations in the Eastern Transvaal Basin (Guo et al., 2009; Luo et al., 2016; Warke and Schröder, 2018; Crockford et al., 2019).

Molybdenum isotope data from other cratons supports the hypothesis of oxidizing shallow water conditions in the late Neoarchean (Duan et al., 2010; Kurzweil et al., 2016; Ostrander et al., 2019). The fractionation in δ^{98}Mo and the negative correlation between Mn concentrations and δ^{98}Mo values observed in these successions are indicative of the presence of Mn oxides in the water column (Planavsky et al., 2014; Kurzweil et al., 2016). It has been recently argued that anticorrelated δ^{98}Mo and ε^{205}Tl records from the Neoarchean Mount McRea Shale in Western Australia require not just the presence of Mn oxides, but stable Mn-oxide burial (Ostrander et al., 2019). However, the first significant Mn deposits do not appear in the sedimentary record for another ~100 million years (Gumsley et al., 2017) in the form of the economically important manganese formations of the Hotazel Formation (Gutzmer and Beukes, 1996; Tsikos et al., 2003; Schneiderhan et al., 2006).

Earlier evidence for Mn oxidation, however, is preserved in the upper Koegas Subgroup (Ghaap Group, Transvaal Supergroup, South Africa; Figure 1). Manganese enrichments of up to 16.1 wt% within diagenetic kutnahorites imply oxidation of Mn^{2+} in depositional environments from ~2430 Ma, even if the cause of Mn^{2+} oxidation remains contested (Beukes and Gutzmer, 2008; Schröder et al., 2011; Johnson et al., 2013; Kurzweil et al., 2016). Kutnahorite is limited to stratigraphically condensed horizons of the Heynskop, Rooinekke, and Naragas formations and has low $\delta^{13}C_{carb}$ values of between -12 and -9 ‰$_{VPDB}$ (Beukes and Gutzmer, 2008; Schröder et al., 2011; Johnson et al., 2013). Manganese enriched kutnahorite formed via the diagenetic reduction of primary Mn^{4+} oxides by organic carbon, and not post-depositional leaching of Mn from sandstones or metasomatism (Johnson et al., 2013). Coupled molybdenum and iron isotope trends in the Rooinekke and Nelani formations imply the presence of Mn oxides and Mo scavenging and shuttling within a redox-stratified water column with Mn oxidation facilitated by free O_2 (Kurzweil et al., 2016). However, Johnson et al. (2013) rejected Mn oxidation by free O_2 on the grounds that deltaic Koegas facies preserve detrital pyrite and uraninite grains and MIF-S signals within detrital and authigenic pyrite; preservation of redox-sensitive detrital grains imply concentrations of atmospheric O_2 of between $1x10^{-7}$ PAL and $3.2x10^{-5}$ PAL (Johnson et al. 2013; 2014). As such, it has been proposed Mn oxidation may have been driven by an ancient, ancestral, Mn-based photosystem (Johnson et al., 2013). However, modelling studies suggest that retention of a reducing atmosphere – generating and transporting S-MIF – is not inconsistent with shallow water oxygen concentrations sufficient for Mn^{2+} oxidation (Olson et al., 2013). Understanding how Mn^{2+} was oxidized during the deposition of the upper Koegas Subgroup will help reconcile the sedimentary occurrences of manganese oxidation with other shallow marine and atmospheric records of oxygenation in the prelude to the Great Oxidation Event (GOE).

Cerium anomalies – both negative and positive – are closely associated with Mn^{2+} oxidation given their similar reduction potentials (Tostevin et al., 2016a; 2016b), catalysis of Ce^{3+} oxidation to Ce^{4+} on the surface of Mn oxides, and immobilization of Ce^{4+} on the surface of particulate Mn oxides (Takahashi et al., 2002). Evidence for Ce oxidation in Koegas strata is mixed. Originally unpublished rare earth element and yttrium (REY_{SN}) values were suggested to show negative cerium anomalies in the iron formations of the Rooinekke Formation, coupled with positive cerium anomalies in interbedded manganiferous carbonates (Beukes et al. 2010), however, a recent study failed to record cerium anomalies, or significant Eu_{SN} anomalies, in carbonates of the upper Koegas Subgroup (Schier et al., 2018).

This contribution further constrains the paleoredox conditions recorded by stromatolitic carbonates in the Koegas Subgroup by integrating the sedimentology, petrography, carbon and oxygen stable isotope systematics, and REY_{SN} characteristics of carbonates from various outcrop sections of the upper Koegas Subgroup.

2. Geological setting

The Koegas Subgroup caps the Ghaap Group (Transvaal Supergroup, South Africa) in the Griqualand West sub-basin and is preserved exclusively to the south-west of the Griquatown growth fault having been either never deposited north-east of the fault, or removed through erosion (Figure 1A; Figure 2; Beukes, 1984; Schröder et al., 2011). The succession unconformably overlies the Griquatown Iron Formation in the east of the sub-basin, but further west the contact becomes conformable (Schröder et al., 2011).

The Koegas Subgroup is comprised of seven formations (Figure 2) of which three – the Doradale, Rooinekke, and Nelani formations – consist of iron formation. Stromatolitic carbonates are present at the contact between the Rooinekke and Heynskop formations, within the Rooinekke-

Nelani iron formations (the Klipputs Member), and near to the contact with the Makganyene Formation (Beukes, 1983;1984; Schröder et al., 2011; Schier et al., 2018). The Koegas Subgroup also hosts secondary, diagenetic carbonates, such as siderite and kutnahorite, which are limited to iron lutite and banded iron formation (BIF) horizons (Schröder et al., 2011).

The majority of the Koegas Subgroup consists of a series of stacked coarsening-upward sequences (KS1-5) which are interpreted as progradational deltaic deposits (Figure 2; Schröder et al., 2011). Iron formations and shales were deposited during transgressive intervals when ferruginous deep waters drowned the delta system (Schröder et al., 2011). Domal stromatolitic carbonates, previously described as limestones (Schier et al., 2018), at the base of the Rooinekke Formation form bioherms that are interpreted as platform margin reefs that were deposited during incipient transgression (Beukes, 1983). Stromatolitic dolostones also occur at the top of Rooinekke Formation, within the Klipputs Member, and were deposited prior to the onset of regression (Beukes, 1983; Schröder et al., 2011; Schier et al., 2018).

The depositional age of Koegas Subgroup has commonly been reported as 2415 ± 6 Ma, based on unpublished zircon Pb-Pb ages obtained from tuff beds in the Rooinekke Formation (Gutzmer and Beukes, 1998). However, these data may have been affected by lead loss and, when corrected, suggest a maximum depositional age of ~2436 Ma (Schier et al., 2018). Alternatively, a Re-Os age of 2479 ± 22 Ma has been obtained from shales within the Klipput Member (Kendall et al., 2013). Both these ages post-date the deposition of the underlying Asbesheuwels Subgroup (~2460 ± 5 Ma to ~2489 ± 33; Nelson et al., 1999; Pickard, 2003), predate the extrusion of the overlying Ongeluk Formation at 2426 ± 3 Ma (Gumsley et al., 2017, and the deposition of the Mooidraai Formation at ~2390 Ma (Bau et al., 1999; Fairey et al., 2013).

The succession has experienced sub-greenschist burial metamorphism (Schröder et al., 2011). On the south-west margin of the Griqualand West sub-basin, Koegas strata are deformed due to crustal shortening accommodated by eastward movement along the Blackridge Thrust Fault during later Proterozoic orogenic episodes that affected the western edge of the Kaapvaal Craton (Beukes and Smit, 1987; Altermann and Hälbich, 1990; 1991).

3. Methods

Samples were collected from measured sedimentary profiles conducted on the farms Taaibosfontein and Sandridge. Polished and stained thin sections (50 μm) were analyzed using transmitted light, reflected light, and cathodoluminescence microscopy. Stained thin sections were treated with alizarin red and potassium ferricyanide. Cathodoluminescence petrography was conducted using a Citl 8200 Mark 2 cold-cathodoluminescence machine (vacuum of ~0.2 Torr, cathode current of 310-335μA, accelerating voltage of 10-12kV). X-ray diffraction (XRD) was performed at the Williamson Research Centre at the University of Manchester using a Bruker D8

Advance diffractometer (Cu Kα X-ray source); samples were scanned from 5 to 70° 2*θ* at a step of 0.02° per 0.2 seconds; results are summarized in Table S3 and discussed in the text and all spectra are shown in the Supplementary Information (Appendix B).

The carbonate digestion protocol used is described by Warke et al. (2018) and is detailed in the Supplementary Inoformation. Sample solutions were analyzed using an Agilent 7500cx inductively coupled plasma mass spectrometer (ICP-MS) and a Perkin-Elmer Optima 5300 dual view inductively coupled plasma atomic emission spectrometer (ICP-AES) at the Williamson Research Centre at the University of Manchester. Four procedural blanks were run for every 50 samples to check for contamination or leaching. Accuracy and precision were monitored using an internal calcite standard and certified reference material TM25.2 (National Water Research Institute, Environment Canada) run after every ten samples, in addition to multi-element standard solutions at a concentration of 1, 5, 10, 50, and 100 ppb for each element analyzed. Relative standard deviation (RSD) for each element analyzed in each sample is shown in Appendix B. Raw REY concentrations were normalized relative to Post Archean Australian Shale (PAAS; Taylor and McLennan, 1985). Results are summarized in Table S4 and S5 included in the Supplementary Information (Appendix B).

Cerium anomalies are calculated by comparing Ce concentrations with the concentrations of the REE with ionic radii closest to that of Ce, i.e. La and Pr (Bau and Dulski, 1996). As La is overabundant in seawater calculation methods that omit La are used (Lawrence and Kamber, 2006; 2007; Lawrence et al., 2006); these equations (Table S2) are used in this contribution and are increasingly used in the redox investigation of Archean-Proterozoic carbonates (e.g. Tostevin et al., 2016a; 2016b; Bellefroid et al., 2018; Hood et al., 2018; Schier et al., 2018; Warke et al., 2018; 2019).

Measurements of carbon and oxygen stable isotopes ($\delta^{13}C$ and $\delta^{18}O$) were conducted on CO_2 which was liberated via phosphorylation and analyzed using a ThermoElemental Delta Plus XL mass spectrometer at the Geologisches-Paläontologisches Institut, Westfälische Wilhelms-Universität in Münster, Germany. Average results based on two replicates of each sample are expressed in the standard delta notation as per mil differences with respect to the Vienna Pee-Dee Belemnite (VPDB; i.e. $‰_{VPDB}$) and are shown in Table S4. Accuracy and precision were monitored by analysis of standard reference materials IAEA-CO-1 (reported $\delta^{13}C$ = 2.492 ± 0.030 $‰_{VPDB}$ and $\delta^{18}O$ = -2.4 ± 0.1 $‰_{VPDB}$) and IAEA-CO-8 (reported $\delta^{13}C$ = -5.764 ± 0.032 $‰_{VPDB}$ and $\delta^{18}O$ = -22.7 ± 0.2 $‰_{VPDB}$). Based on 16 measurements of both standards, the average value for IAEA-CO-1 was $\delta^{13}C$ = 2.50 ± 0.024 $‰_{VPDB}$ and $\delta^{18}O$ = -2.4 ± 0.04 $‰_{VPDB}$ and the average value for IAEA-CO-8 was $\delta^{13}C$ = -5.764 ± 0.032 $‰_{VPDB}$ and $\delta^{18}O$ = -22.7 ± 0.02 $‰_{VPDB}$. All standard and sample data are shown in the Supplementary Information (Appendix B).

4. Results

4.1 Field, petrographic, and mineralogical observations

Three sections through the Naragas, Heynskop, and Rooinekke formations (and in section TBF-A only, the Makganyene Formation) were measured on the farm Taaibosfontein. Stromatolitic bioherms occur at the transition between the Heynskop and Rooinekke formations, forming an ~20-cm-thick marker horizon that can be traced for ~2 km (Figure 3). At infrequent intervals this bed thickens due to the development of small (1-1.5 m high, 2-3 m wide) stromatolite bioherms (Figure 4A, 4B).

Section TBF-C (Figure 3), the longest section measured through the succession on Taaibosfontein, starts with 30-60 cm thick beds of planar-laminated, orange-pink, weathered, fine-to-medium grained sandstones of sublitharenite to litharenite composition (depending on the ratio of angular quartz grains to chert, plagioclase, and microcline). From ~29 to 55 m, section TBF-C alternates between fine-grained, blue-grey sandstones and chlorite-rich mudstone. Blue-grey sandstones have a lithic greywacke composition with a matrix rich in chlorite (up to 24 modal%) and contain rounded pyrite grains up to 200 μm in diameter (Figure 5A, 5B). They occur in cm-dm thick beds, fine upwards, and have erosive bases. In all sections the blue-grey sandstone beds, which are interbedded with mudstones, are overlain by iron-rich mudstones (iron lutite) with siderite nodules 1-2 cm in diameter and cm-thick chert beds. Recessively weathered, goethite-rich iron lutite is interbedded with: (i) mudstones; (ii) cm-thick, cross-bedded, fine-grained sandstone beds; and (iii) stromatolitic carbonate. Iron lutite beds pass gradationally into BIF.

Stromatolitic carbonates consist of non-ferroan calcite, ferroan calcite and dolomite, as identified from stained thin sections. XRD spectra lack the distinct ordering peaks of dolomite, but ankerite is detected. These carbonates are recrystallized and the contact between areas of ferroan calcite and dolomite is gradational with no change in crystal shape and size. Bands of ferroan dolomite and ferroan calcite follow bedding lamination in some areas, but in other areas the distribution of dolomite is more random and the dolomitization front cross cuts bedding lamination. Ferroan dolomite crystals have a monotonous red-orange luminescence with brighter orange-yellow rims (Figure 5F). Some areas are dominated by an unstained, non-luminescent, rhombal dolomite with a planar-e fabric with red-orange rims. Coarsely crystalline calcite veins show bright yellow-orange luminescence. Clasts of quartz, chert, and micritic peloids, are concentrated along dissolution seams and immature stylolites (Figure 5C). Euhedral magnetite and pyrite overprint planar-s dolomite.

Similar facies relationships are observed on the farm Sandridge 191, but exposure is generally limited to the iron lutite, stromatolitic carbonate, and BIF beds (Figure 6). On Sandridge, the stromatolitic carbonates form 1.65-2.85 m thick beds which are laterally continuous for ~650 m. Sandridge carbonates are predominately ferroan dolomite and a persistent crinkly lamination but do not form domal bioherms like on Taaibosfontein. Small domes up to 3 cm high and 6-10 cm in diameter are seen (Figure 4D-F). In thin section a fine-grained mauve-stained ferroan calcite population (< 20 μm) with a bright orange-yellow luminescence is restricted to isolated pockets which are enclosed by elongate to bladed silica crystals (Figure 4D; 7A-B). Progressive, inward, fabric-retentive dolomitization of these pockets is observed. A coarser-grained turquoise stained ferroan dolomite (~ 50 -100 μm) population makes up the majority of the observed carbonate and possesses either a dull red luminescence or is non-luminescent (Figure 7B). Dissolution seams, which are spatially associated with overprinting chlorite (~1 %) and riebeckite (1-10 %) (Figure 7C), commonly cross-cut the carbonates. Riebeckite crystals are in turn cross-cut by carbonate veins (Figure 7D).

4.2 Major and trace element analysis

Carbonates from Taaibosfontein have Mn, Mg and Fe concentrations that range from 0.9 to 2.1 %, 0.3 to 6.4 %, and 1.4 to 9.4 %, respectively (Table S4). Strontium concentrations range from 13 to 276 ppm but are typically between approximately 100 and 200 ppm. Manganese and strontium concentrations show a weak negative correlation (Figure S1). Sandridge carbonates have higher concentrations of Mg (0.2 to 5.9 %) and Fe (3.6 to 12.9 %) than on Taaibosfontein, but Mn concentrations are lower (1741 to 3931 ppm). Strontium concentrations vary from 55 to 460 ppm and show no systematic variation with Mn concentration. Al concentrations in Taaibosfontein carbonates are generally higher (103 to 2331 ppm) than in Sandridge carbonates (67 to 1347 ppm).

4.3 REY_{SN} patterns and Ce_{SN} anomalies

Ferroan carbonates from Taaibosfontein and Sandridge show little evidence for detrital contamination using REY_{SN} ratios, i.e. $(La/Sm)_{CN} > 1$, $(Sm/Yb)_{SN} < 1$, and $(Eu/Sm)_{SN} > 1$. Taaibosfontein carbonates do show a weak positive correlation between ΣREE and Al and Th possibly indicating some detrital influence on the REY_{SN} signal (Figure S2), but Sandridge dolostones show constant ΣREE values regardless of Al, Ti or Th concentration (Figure S3). Carbonates from both localities show HREE enrichment and Y/Ho ratios that are either superchondritic (>40) or exceed chondritic values (>27) (Figure 8). Positive La_{SN} and Gd_{SN} anomalies are calculated in most samples (Table S5). Positive Eu_{SN} anomalies are noted in samples from Taaibosfontein and Sandridge and can be visually identified from the REY_{SN} array (Figure 8). No significant negative Ce_{SN} anomalies are noted in either Taaibosfontein or Sandridge samples (Table S5; Figure 9), however, positive anomalies are noted from both sites. Eight samples from Taaibosfontein show $(Ce/Ce^*)_{SN}$ values ≥ 1.1; four samples show $(Ce/Ce^*)_{SN}$ values ≥ 1.3 (Figure 9). On Sandridge, 21 samples record $(Ce/Ce^*)_{SN}$ values ≥ 1.1 and six record $(Ce/Ce^*)_{SN}$ values ≥ 1.3 (Figure 9; Table S5).

During sample ionization oxides and hydroxides of Ba can form which interfere with Eu^{131} and Eu^{135} (Jarvis et al., 1989). This can lead to overestimation of Eu concentrations and therefore lead to the calculation of artificial positive Eu_{SN} anomalies. This effect, however, is only significant in Ba-rich rocks and in the case of most geological materials no correction is necessary (Jarvis et al., 1989). Where Ba/Eu ratios are <1000 Ba interference is not generally considered to have strongly affected the Eu concentrations (Kent and Ungerer, 2005). A sub-set of Sandridge and Taaibosfontein carbonates have an average Ba/Eu ratio of 321 (n=11; see SI) with most samples in the range of 13 to 260; only one sample has a Ba/Eu ratio exceeding 1000. Interference can also be monitored by a positive correlation between Eu/Eu^*_{SN} values and Ba/Sm ratios (Tostevin et al., 2016a). No correlation between these two variables is evident (Figure S4), suggesting the Eu/Eu^*_{SN} values are a real feature of the samples.

4.4 Carbon and oxygen stable isotope analysis

The stromatolitic bioherms on the farm Taaibosfontein yield $\delta^{13}C_{carb}$ values of -6.92 to -2.85 ‰$_{VPDB}$ (mean: -4.7 ‰$_{VPDB;}$ n=18) and $\delta^{18}O_{carb}$ values of -18.26 to -11.53 ‰$_{VPDB}$ (mean: -13.7 ‰$_{VPDB}$; n=18) (Table S4; Figure 10). Crinkly laminated ferroan dolostones on Sandridge have $\delta^{13}C_{carb}$ values which range from -8.00 to -3.99 ‰$_{VPDB}$ (mean: -5.6 ‰$_{VPDB}$; n=25) and $\delta^{18}O_{carb}$ values of between -13.35 and -4.79 ‰$_{VPDB}$ (mean: -11.7 ‰$_{VPDB}$; n=25) (Figure 10). Taaibosfontein carbonates show a strong correlation between higher relative Fe/Ca ratios and lower $\delta^{13}C_{carb}$ values (R=0.87; n= 16) and to a lesser extent correlation between higher relative Mg/Ca ratios and lower $\delta^{13}C_{carb}$ values (R=0.67; n=16) (Figure S5). There is no correlation between Mn/Ca ratios and $\delta^{13}C_{carb}$ values. On Sandridge, similar correlations are broadly noted but they are weaker. No significant correlation between $\delta^{18}O_{carb}$ values and element ratios is observed.

5. Discussion

5.1 The paragenetic evolution of upper Koegas Subgroup carbonates

Recrystallized, domal stromatolitic facies on Taaibosfontein consist of a mixture of ferroan dolostone and ferroan limestone and have a mean $\delta^{13}C_{carb}$ value of -4.7 ‰$_{VPDB}$ (n=18) and a mean $\delta^{18}O_{carb}$ value of -13.7 ‰$_{VPDB}$ (n=18). Crinkly laminated stromatolitic beds on Sandridge consist of recrystallized ferroan dolomite, with limited pockets of ferroan calcite, and have a mean $\delta^{13}C_{carb}$ value of -5.6 ‰$_{VPDB}$ (n=24) and a mean $\delta^{18}O_{carb}$ value of -12.0 ‰$_{VPDB}$ (n=24). The sub-millimeter carbonate heterogeneity observed here in thin section – and confirmed by bulk rock XRD – differs from previous studies which have described the Taaibosfontein and Sandridge bioherms as limestones and dolostones, respectively (Schier et al., 2018). A more complicated paragenetic history is evident (Figure 11), suggesting that bulk rock analyses may reflect a mixing of different carbonate types. The mixing of ferroan dolomite and ferroan calcite in bulk rock powders, in addition to the high iron content of these carbonates, may in part explain why Mg/Ca ratios are lower than expected for typical dolostones. As ferroan dolomite tends to dominate samples from both localities, in the following discussion the term “dolostone” is used but a significant degree of fine-scale heterogeneity is implied in all samples. For instance, in all but two samples from Taaibosfontein and Sandridge, Fe/Ca ratios equal or exceed Mg/Ca ratios implying that these carbonates may lie between ferroan dolomite and ankerite in composition; the latter phase is evident from XRD spectra, while ferroan dolomite is identified in thin-section.

REY_{SN} trends in carbonates from the upper Koegas Subgroup can be used to test for shallow marine oxygenation of Mn^{2+} and redox stratification of the basin. The determination of Ce_{SN} anomalies provides qualitative, and in some cases quantitative, constraint on the dissolved oxygen concentration in ambient seawater (Bellefroid et al., 2018). REY_{SN} anomalies, however, can only be reliably interpreted in carbonates that lack detrital contamination (Bau and Dulski, 1996) and that preserve marine REY_{SN} patterns that consist of: (i) depleted light REE (LREE); (ii) positive anomalies of La_{SN} and Gd_{SN}, (Bau and Dulski, 1996), and; (iii) superchondritic Y/Ho ratios of ~40-90, which is indicative of marine fractionation (Allwood et al., 2010). Primary marine REY_{SN} patterns and anomalies can be retained through diagenesis (Voigt et al., 2017), dolomitization (Liu et al., 2019), and even high-temperature metamorphism in circumstances where the fluid to rock ratio likely remained low (Baker and Fallick, 1989a; 1989b; Warke et al., 2018; Cabral et al., 2019), as REY_{SN} patterns and anomalies can be reset at high fluid to rock ratios of >10^3 (Banner et al., 1988; Tostevin et al., 2016a). To assess the probability of carbonate-fluid interaction, REY_{SN} analysis should be coupled with detailed petrographic investigation (Hood et al., 2018).

The carbonates on Taaibosfontein preserve marine REY_{SN} arrays that display HREE enrichment, superchondritic Y/Ho ratios and positive anomalies of La_{SN} and Gd_{SN}. There is some evidence (ΣREE vs Al and Th concentration) that there may have been a minor detrital influence on Taaibosfontein REY_{SN} patterns, however a marine REY_{SN} pattern is still dominant. This is in broad agreement with previous work, with the exception that positive Eu_{SN} anomalies are noted in this study and not by Schier et al. (2018). Sandridge dolostones show no evidence of detrital contamination and preserve robust marine REY_{SN} arrays despite evidence for their interaction with one or more riebeckite-precipitating fluids during burial (syn or post-compaction and stylolite formation); previous studies fail to record marine REY_{SN} arrays from Sandridge (Schier et al. (2018).

The stable isotope values and element (Mn, Fe, Sr, Mg) concentrations measured from Taaibosfontein and Sandridge dolostones are in close agreement with other studies (Frauenstein et al., 2009; Schier et al., 2018). The Mn concentrations measured are elevated relative to average Paleoproterozoic seawater values (~0.5 %; Veizer et al., 1992), attaining maximum values of 2.1 % in Taaibosfontein carbonates. Iron content is also elevated in these carbonates relative to Paleoproterozoic seawater (~1.2 %; Veizer et al.,1992). It is reasonable to assume that the marine REY_{SN} patterns and anomalies (particularly superchondritic Y/Ho) imply that these carbonates precipitated from early Paleoproterozoic seawater and, as such, initially recorded a $\delta^{13}C_{carb}$ value of ~0 ‰$_{VPDB}$ and a $\delta^{18}O_{carb}$ of ~ -7 ‰$_{VPDB}$ (Veizer et al., 1992; Shields and Veizer, 2002; Prokoph et al., 2008) and elevated seawater Fe, Mn and Mg concentrations. If correct, this suggests that Upper Koegas carbonates are relatively depleted in $\delta^{13}C_{carb}$ by ~5 ‰$_{VPDB}$ on average, and in some cases by up to ~7 ‰$_{VPDB}$. The $\delta^{18}O_{carb}$ is commonly depleted by ~5 to ~7‰$_{VPDB}$ on average in comparison to estimated seawater values, however it is easier to lower oxygen isotope values during diagenesis as oxygen is more readily exchanged between the host rock and oxygen-rich fluids (H_2O, CO_2) than carbon which is rock buffered. It is possible that the $\delta^{13}C_{carb}$ values could reflect localized, primary values in a $\delta^{13}C$ depleted water column that was spatially isolated from the ocean, however the correlations of lower $\delta^{13}C_{carb}$ with increasing Sr concentrations and increasing Mg/Ca and Fe/Ca ratios suggest that diagenetic processes have principally controlled metal concentrations and isotope values.

Thermal alteration may explain part of the isotopic depletion, however, as this process typically causes covariation between $\delta^{13}C_{carb}$ and $\delta^{18}O_{carb}$ values as temperature increases (Choquette and James, 1987) and no such covariation is observed at Taaibosfontein and Sandridge (Figure 10), additional depletion mechanisms are implied.

The lowering of $\delta^{13}C_{carb}$ and concomitant increase in Fe/Ca, Mg/Ca and Sr could have been caused by interaction with and recrystallization from a ferruginous ^{12}C-rich fluid during burial. This fluid may have been sourced from the diagenetic reduction of iron-oxhydroxides by organic matter in the adjacent iron lutite and BIF deposits. Dissimilatory iron reduction would have produced diagenetic fluids rich in reduced Fe, Mg, and Mn, in addition to $\delta^{13}C_{carb}$ depleted bicarbonate (Posth et al., 2013; Fairey et al., 2013). Circulation of these fluids in the lutitic and arenitic lithologies of the Koegas may also have contributed Sr, which was incorporated to the precipitated carbonate. Marine REY_{SN} characteristics may have been retained due to the greater resilience afforded to REY by their substitution for Ca^{2+} in the carbonate lattice (Voigt et al., 2017; Liu et al., 2019).

As these recrystallization fabrics are cross-cut and crystals truncated by dissolution seams and proto-stylolites it is probable that fluid interaction and recrystallization occurred prior to significant burial as stylolites can form within the first kilometer of burial (Figure 11). On Sandridge, a fine-grained calcite population has been preserved in isolated pockets that are enclosed by silica (Figure 6A). These fine-grained crystals may represent an earlier phase that has been protected against a later dolomitization and recrystallization, perhaps by early diagenetic silicification.

Point counting shows that Sandridge dolostones contain up to 10 % riebeckite. The formation of riebeckite within iron formations of the Transvaal Supergroup is the result of diagenetic reactions in Griqualand West (Tsikos and Moore, 1997) and diagenetic and metasomatic processes in the Transvaal Basin (Miyano and Beukes, 1997; Warke et al., 2018), however, it is seldom noted in carbonates. Syndepositional to early-diagenetic riebeckite is described from the Mooidraai-Hotazel transition where its formation is attributed to increased salinity in the water column and in pore fluids at the interface between the BIF and carbonate depositional environments (Fairey et al., 2013). Hence, some of the observations presented could support the existence, at least transiently, of an evaporitic setting. In addition to explaining the initial source of Na (Fairey et al., 2013), it is possible that bladed silica may represent replacement of a sulfate precursor. The first appearance of evaporitic sulfates (and pseudomorphs) are not noted until the late Paleoproterozoic (Schröder et al., 2008; Blättler et al., 2018), however recently evaporites dating to ~2310 Ma have been discovered in the Transvaal Supergroup (Crockford et al., 2019).

While evaporitic conditions remain a possibility that should be assessed in future studies, a stratigraphically controlled Na^+ source does not best explain the riebeckite distribution in the Sandridge carbonates, where riebeckite occurs only in close spatial association with dissolution structures. It is more likely that riebeckite formation occurred in response to circulation of Na^+ rich metasomatic fluids after host rock recrystallization (Figure 11). Riebeckite is only noted at Sandridge, and not at Taaibosfontein, suggesting that the fluids responsible were only locally circulated, possibly along faults.

The occurrence of chlorite along dissolution structures further suggests that they acted as conduits for the movement of hydrous, diagenetic fluids. Euhedral iron oxides overprint the riebeckite and must be attributable to a later iron-rich fluid. Thin calcite veins cross-cut riebeckite crystals and, with bright yellow luminescence, stand in sharp contrast to the very dull to non-luminescent host carbonate. Euhedral pyrite crystals are diagenetic in nature and postdate the second carbonate recrystallization but their timing relative to the dissolution seams and associated precipitates is unconstrained.

5.2 Cerium anomalies

Negative Ce_{SN} anomalies in seawater result when O_2 concentrations are sufficiently high to oxidize soluble Ce^{3+} and stabilize it as insoluble Ce^{4+} (Elderfield, 1988). This reaction is catalyzed on the surfaces of Mn^{4+}-oxyhydroxide/oxides where Ce^{4+} is immobilized (Takahashi et al., 2000). Cerium oxidation may also be facilitated on the surface of Fe^{3+} oxyhydroxide/oxides (Bau, 1999; Bau and Koschinsky, 2009), but the evidence for this is less consistent than catalysis on Mn-oxyhydroxide/oxide surfaces (Loges et al. 2012). Upon burial of the oxidized particulates, the water column becomes anomalously depleted in Ce; this depletion is transferred to authigenic carbonate from the water column. Positive Ce_{SN} anomalies are generated when oxygen concentrations are high enough to facilitate Ce^{3+} oxidation in surface waters, but oxygen is limited lower in the water column, i.e. it is redox-stratified (Tostevin et al., 2016b). Sinking of oxidized particulates into lower oxygen zones in the water column and the sediment-water interface results in the reduction of the (now unstable) Ce^{4+} and manganese oxyhydroxides/oxides (Tostevin et al., 2016b; Ostrander et al., 2019). This release of reduced Ce^{3+} causes an anomalous enrichment (positive anomaly) at depth that is transferred to locally precipitating carbonate (Planavsky et al., 2010; Tostevin et al., 2016b).

As discussed above, Ce_{SN} anomalies are calculated using equations that omit reference to La as La is overabundant in seawater (Lawrence and Kamber, 2006; 2007; Lawrence et al., 2006). However, these equations can underestimate Ce concentrations producing artificial positive Ce_{SN} anomalies of ~20 % (Kamber et al., 2014). Consequently, $(Ce/Ce^*)_{SN}$ values > 1.1 but < 1.3 could indicate positive anomalies but should be interpreted cautiously, however values > 1.3 are likely to be true positive anomalies (Tostevin et al., 2016b).

Iron formations within the Koegas Subgroup have been reported to show negative Ce_{SN} anomalies, while carbonates in the upper portion of the succession may record positive Ce_{SN} anomalies (Beukes et al., 2010). However, a more recent study found variable marine and non-marine REY_{SN} patterns, lacking Ce_{SN} and Eu_{SN} anomalies, which were interpreted as evidence that shallow marine environments were insufficiently oxygenated to oxidize Ce^{2+} (Schier et al., 2018). These authors argued that the contribution of hydrothermal waters to shallow marine environments waned at ~2436 Ma causing disappearance of the positive Eu_{SN} anomaly noted in Neoarchean shallow water carbonates (Beukes and Gutzmer, 2008).

Carbonates from Taaibosfontein and Sandridge preserve marine REY_{SN} arrays that display HREE enrichment, superchondritic Y/Ho ratios and positive anomalies of La_{SN}, Gd_{SN}, and Eu_{SN} (total of 46 samples). As discussed above, Ce_{SN} anomalies were calculated using the equations of Lawrence and Kamber (2006; 2007), but these equations can underestime the predicted Ce concentration and thus lead to calculation of false positive anomalies of Ce_{SN} of around ~20 % (Kamber et al., 2014). Cautious interpretation, therefore, requires that definitive positive anomalies of $(Ce/Ce)_{SN}$ are restricted to values exceeding 1.3 (Tostevin et al., 2016b). No significant negative cerium anomalies are detected at any locality, however, positive anomalies (>1.1) are noted in almost all samples (83 %) and eight samples (17%) have $Ce/Ce^*)_{SN}$ values > 1.3. This finding supports the unpublished positive Ce_{SN} anomalies in Koegas carbonates first noted by Beukes et al. (2010), but contrasts with the findings of Schier et al. (2018) who found no Ce or large Eu anomalies.

5.3 Was the Koegas basin redox stratified?

Redox stratification of the Koegas basin has also been inferred from variations in $\delta^{56}Fe$, $\delta^{98}Mo$ and Mn concentrations in Koegas BIF facies which correlate with sea-level fluctuations (Kurzweil et al., 2016). The preferential adsorption of isotopically light Mo onto the surface of sinking Mn^{4+} oxides, shuttles low $\delta^{98}Mo$ to deeper waters (Alego and Tribovillard, 2009; Scholz et al., 2013). Settled Mn oxides are incorporated into sediment at the Mn redoxcline following the reduction of

Mn oxides; this elevates sediment Mn concentrations just below the Mn redoxcline (Kurzweil et al., 2016; Albut et al., 2019). This model postulates that Mn^{4+} oxides formed as a result of the interaction of dissolved Mn^{2+} with free O_2 in the water column (Kurzweil et al., 2016), as was also proposed by Planavsky et al. (2014) for successions displaying negative correlation between δ^{98}Mo and Mn concentration. Additionally, in the Nelani Formation, the negative correlation of Mn concentrations with δ^{56}Fe values suggests that Fe fractionation is associated with Mn oxide formation (Kurzweil et al., 2016). It is suggested that the formation of Fe^{3+} oxyhydroxides along the Mn redoxcline is related to the upward diffusion of Fe^{2+} due to O_2 consumption by Mn^{2+} oxidation, and the stepwise replacement of Mn^{4+} by Fe^{3+} in particulate Mn^{4+} oxides (Dellwig et al., 2010; Kurzweil et al., 2016). As Fe^{3+} oxyhydroxides are isotopically heavy, their export to deeper waters causes sediment deposited below the Mn redoxcline to incorporate the resultant pool of isotopically lighter δ^{56}Fe.

Given the relationship between Mn and Ce oxidation outlined above, the Mn-shuttle model can also predict the behavior of Ce within a redox-stratified water-column (Figure 12; Planavsky et al., 2010; Tostevin et al., 2016b). The presence of positive Ce_{SN} has been considered an essential criterion for inferring the operation on a Mn-shuttle and redox-stratification within a basin (Planavsky et al., 2010). The oxidation of Mn^{2+} above a Mn^{4+}/Mn^{2+} redoxcline redoxcline leads to the formation of insoluble Mn^{4+} oxides, which catalyze the oxidation of Ce^{3+} (Bau et al., 1999). As particulate oxides sink through a redox stratified water column the reduction of Mn^{4+} oxides (and thus Ce^{4+}) at the $Mn^{2+/4+}$ redoxcline lead to an enrichment in Mn and Ce in carbonates deposited below the redoxcline, in addition to elevated Mn/Fe ratios (Tostevin et al., 2016b). The sediment deposited just above the boundary between oxic and manganous waters should contain Mn enrichment that is coincident with low δ^{98}Mo values, low δ^{56}Fe values and negative Ce_{SN} anomalies. Positive anomalies of Ce_{SN} are expected below this boundary due to the reduction of Ce^{4+} to Ce^{3+} in the water column, which is then incorporated into carbonate precipitating at this depth (Figure 12; Tostevin et al., 2016b).

Therefore, $(Ce/Ce^*)_{SN}$ values > 1.1 (and less ambiguously >1.3) indicate redox cycling during the deposition of the Klipputs Member (Sandridge) and along the contact between the Heynskop and Rooinekke formations (Taaibosfontein) and add support for the redox stratification model of Kurzweil et al. (2016) and independent evidence for the operation of the Mn-oxide shuttle. While upper Koegas dolostones with marine REY_{SN} patterns and positive Ce_{SN} anomalies contain Mn contents up to 2.1 wt%, Mn/Fe ratios are not significantly elevated, reflecting the addition of iron during diagenesis rather than low Mn concentrations, as discussed previously.

The formation of primary Mn^{4+} oxides in the Koegas basin also explains high Mn concentrations (up to 16.1 w%) in authigenic kutnahorite horizons within the upper Koegas iron formations (Beukes and Gutzmer, 2008; Schröder et al., 2011; Johnson et al., 2013). Kutnahorite horizons possess depleted $\delta^{13}C_{carb}$ values of between -12 and -9 ‰$_{VPDB}$ and are restricted to condensed portions of the Rooinekke, Naragas, and Heynskop formations, where slow sedimentation rates allowed for the accumulation of sedimentary Mn^{4+} oxides in the sediment (Johnson et al., 2013). Observed Mn concentrations are considered too high to be explained by Mn^{2+} incorporation into the primary carbonate during precipitation, rather kutnahorite is considered to have formed via the diagenetic reduction of Mn oxides by burial fluids rich in organic carbon, thus also causing the observed $\delta^{13}C_{carb}$ depletion in kutnahorites (Johnson et al., 2013). This interpretation is supported by a negative correlation between δ^{98}Mo values and Mn concentrations in Koegas BIF deposits (Kurzweil et al., 2016). A similar mechanism of secondary, diagenetic Mn-carbonate formation (and enrichment) has been identified in the iron and manganese formations of the Hotazel Formation (Tsikos et al., 2003; Schneiderhan et al., 2006).

The initial mechanism of Mn^{2+} oxidation, however, is contested. It was previously argued that the oxidation of Mn^{2+} by photosynthetically derived free oxygen is incompatible with the retention of detrital pyrite and uraninite, and mass-independently fractionated sulfur isotopes (S-MIF), in the Koegas Subgroup (Johnson et al., 2013). Rather, it was proposed that the only viable mechanism of Mn oxidation was a previously unrecognized high-potential photosystem (Johnson et al., 2013). However, for this Mn-oxidation pathway to be probable it must be demonstrated that free oxygen can be excluded as a high-redox-potential oxidant (Jones and Crowe, 2013).

S-MIF signals record atmospheric photochemical reactions and S-MIF magnitudes reflect the proportion of different reduced and oxidized sulfur aerosol exit pathways from the atmosphere (Farquhar et al., 2000; Claire et al., 2014). In a reducing atmosphere, these pathways can be kept separate and S-MIF signals are incorporated into the rock record, however after the GOE the oxygenation of the atmosphere leads to oxidation of reduced aerosols and homogenization of the exit pathways into one sulfate pool which erases the S-MIF signal (Claire et al., 2014). Ample evidence supports transient oxygen production and accumulation in Archean shallow water environments under a reducing atmosphere that generated S-MIF and allowed transportation and deposition of reduced, S-MIF carrying aerosols (Anbar et al., 2007; Garvin et al., 2009; Godfrey and Falkowski, 2009; Kendall et al., 2010; Voegelin et al., 2010; Ostrander et al., 2019; Albut et al., 2019). It also remains unclear to what extent the disappearance of S-MIF in the rock record reliably records atmospheric and shallow-water oxygenation both temporally and spatially (Reinhard et al., 2013; Philippot et al., 2018). Thus, S-MIF preservation is not sufficient grounds to argue against oxygen accumulation in shallow water environments.

Detrital pyrite is limited to shallow water, delta top sandstones (Johnson et al., 2013; 2014) and prodelta turbidites within the Naragas and Heynskop formations (Figure 2; 6B). These progradational deltaic sandstones represent periods of increased siliciclastic input into the basin and enhanced sedimentation rates (cycles KS2-4: Schröder et al., 2011). In contrast, the Mn oxides are considered to have been deposited in transgressive and high-stand systems tracts, within condensed sections (Johnson et al., 2013). Detrital pyrite occurrences are therefore not coincident with the sequence stratigraphic position of the Mn enrichments. Detrital pyrite oxidation occurs at trace O_2 levels (Johnson et al. 2014), including levels likely to have been locally generated by early Proterozoic oxygen oases (Olsen et al., 2013; Lalonde and Konhauser, 2015). However, the rapid transport and burial of sediment in deltaic deposits, coupled with the spatiotemporal separation of sites of oxygen production from sites of clastic deposition, may also have limited pyrite oxidation in shallow marine environments. Evidence for redox stratification occurs during depositional cycle KS5, which is comprised of the Rooinekke and Nelani formations (Figure 2); these formations lack detrital pyrite deposits (Kurzweil et al., 2016).

Therefore, important spatiotemporal differences exist between the depositional environments that preserve the evidence for Mn oxidation and those that preserve detrital pyrite and S-MIF signals. This means that the preservation of these signals in the Koegas Subgroup cannot be used to argue against the existence of free oxygen and in favour of a Mn-based photosystem. Redox stratification of the basin provides a more plausible explanation of Mn oxidation.

6. Conclusions

This study presents detailed and integrated sedimentological, petrographic, and geochemical study of the stromatolitic carbonates in the upper Koegas Subgroup. Stromatolitic carbonates from across the sub-basin record similar characteristics: depleted $\delta^{13}C_{carb}$ and $\delta^{18}O_{carb}$ values which are associated with iron-rich carbonate minerals and elevated Fe-concentrations. It is suggested that early in the paragenetic evolution of these carbonate successions, precursor carbonate phases interacted with ^{13}C depleted Fe-carbonate fluids derived from the reduction of Fe^{3+} oxides by organic carbon in the adjacent BIF and iron lutite deposits. Despite some evidence for diagenetic alteration, marine REY_{SN} patterns are preserved in heterogeneous stromatolitic carbonate facies on the farms Taaibosfontein and Sandridge. These carbonates do not record significant negative Ce_{SN} anomalies, although small positive Ce_{SN} anomalies are noted. While some positive Ce_{SN} anomalies calculated here may be calculation artifacts, values > 1.3 may indicate redox cycling of Mn and Ce across a Mn redoxcline. This implies that the Koegas basin was redox stratified, as was proposed by Kurzweil et al. (2016) on the basis of Fe and Mo isotope trends coupled with Mn concentrations within the Nelani Formation. This model proposes that Mn oxide formation in the Koegas Formation was caused by interaction of dissolved Mn^{2+} with free O_2 in surface waters and not photooxidation of Mn^{2+} facilitated by an ancient bacterial photosystem (Johnson et al., 2013).

Acknowledgements

N. Beukes and J. Lavi provided field support and discussion. S. Polteau provided locality information. MRW was supported by a NERC-studentship through the University of Manchester (NEL501591/1) and by the REI Fund of the Geological Society of South Africa. SS was supported through a Strategy Grant of the Faculty of Engineering and Physical Sciences at the University of Manchester. P. Lythgoe and J. Waters are thanked for help with the ICP-MS/AES and XRD analyses respectively. We thank an anonymous reviewer and Alexandre Raphael Cabral for their constructive and thoughtful reviews which improved the manuscript.

7. References

Albut, G., Kamber, B.S., Brüske, A., Beukes, N.J., Smith, A.J. and Schoenberg, R., 2019. Modern weathering in outcrop samples versus ancient paleoredox information in drill core samples from a Mesoarchaean marine oxygen oasis in Pongola Supergroup, South Africa. *Geochimica et Cosmochimica Acta*, **265**, 330-353.

Allwood, A.C., Kamber, B.S., Walter, M.R., Burch, I.W. and Kanik, I. 2010. Trace elements record depositional history of an Early Archean stromatolitic carbonate platform. *Chemical Geology*, **270,** 148-163.

Altermann, W. and Hälbich, I.W.1990. Thrusting, folding and stratigraphy of the Ghaap Group along the southwestern margin of the Kaapvaal Craton. *South African Journal of Geology,* **93**, 553-566.

Altermann, W. and Hälbich, I.W. 1991. Structural history of the southwest corner of the Kaapvaal Craton and the adjacent Namaqua realm: new observations and a reappraisal. *Precambrian Research*, **52**, 133-166.

Anbar, A.D., Duan, Y., Lyons, T.W., Arnold, G.L., Kendall, B., Creaser, R.A., Kaufman, A.J., Gordon, G.W., Scott, C., Garvin, J. and Buick, R. 2007. A Whiff of Oxygen Before the Great Oxidation Event? *Science*, **317**, 1903-1906.

Baker, A.J. and Fallick, A.E., 1989a. Heavy carbon in two-billion-year-old marbles from Lofoten-Vesterålen, Norway: Implications for the Precambrian carbon cycle. *Geochimica et Cosmochimica Acta*, **53**, 1111-1115.

Baker, A.J. and Fallick, A.E., 1989b. Evidence from Lewisian limestones for isotopically heavy carbon in two-thousand-million-year-old sea water. *Nature*, **337**, 352-354.

Banner, J.L., Hanson, G.N. and Meyers, W.J. 1988. Rare earth element and Nd isotopic variations in regionally extensive dolomites from the Burlington-Keokuk Formation (Mississippian): Implications for REE mobility during carbonate diagenesis. *Journal of Sedimentary Petrology*, **58,** 415-432.

Bau, M. 1999. Scavenging of dissolved yttrium and rare earths by precipitating iron oxyhydroxide: experimental evidence for Ce oxidation, Y-Ho fractionation, and lanthanide tetrad effect. *Geochimica et Cosmochimica Acta*, **63,** 67-77.

Bau, M. and Dulski, P. 1996. Distribution of yttrium and rare-earth elements in the Penge and Kuruman iron-formations, Transvaal Supergroup, South Africa. *Precambrian Research*, **79**, 37-55.

Bau, M. and Koschinsky, A. 2009. Oxidative scavenging of cerium on hydrous Fe oxide: evidence from the distribution of rare earth elements and yttrium between Fe oxides and Mn oxides in hydrogenetic ferromanganese crusts. *Geochemical Journal*, **43,** 37-47.

Bellefroid, E.J., Hood, A.V.S., Hoffman, P.F., Thomas, M.D., Reinhard, C.T. and Planavsky, N.J., 2018. Constraints on Paleoproterozoic atmospheric oxygen levels. *Proceedings of the National Academy of Sciences*, **115**, 8104-8109.

Beukes, N.J. 1983. Palaeoenvironmental setting of iron-formations in the depositional basin of the Transvaal Supergroup, South Africa. In: Trendall, A.F. and Morris, S.C. (Eds), *Iron Formation: Facts and Problems.* Elsevier, Amsterdam, pp 131-209.

Beukes, N.J. 1984. Sedimentology of the Kuruman and Griquatown iron-formations, Transvaal Supergroup, Griqualand West, South Africa. *Precambrian Research*, **24**, 47-84.

Beukes, N.J. and Smit, C.A. 1987. New evidence for thrust faulting in Griqualand West, South Africa: implications for stratigraphy and the age of red beds. South African Journal of Geology, 90, 378–394.

Beukes, N.J. and Gutzmer, J. 2008. Origin and paleoenvironmental significance of major iron formations at the Archean-Paleoproterozoic boundary. *Reviews in Economic Geology*, **15**, 5-47.

Beukes, N.J., Gutzmer, J. and Nel, B.P. 2010. Ce anomalies in ~2.4 Ga iron and manganese formations as a proxy for early oxygenation of oceanic environments (abstract). *Geochimica et Cosmochimica Acta*, **74**, A85**.**

Blättler, C.L., Claire, M.W., Prave, A.R., Kirsimäe, K., Higgins, J.A., Medvedev, P.V., Romashkin, A.E., Rychanchik, D.V., Zerkle, A.L., Paiste, K. and Kreitsmann, T., 2018. Two-billion-year-old evaporites capture Earth's great oxidation. *Science*, **360**, 320-323.

Cabral, A.R., Zeh, A., Vianna, N.C., Ackerman, L., Pašava, J., Lehmann, B. and Chrastný, V., 2019. Molybdenum-isotope signals and cerium anomalies in Palaeoproterozoic manganese ore survive high-grade metamorphism. *Scientific Reports*, **9**, 1-7.

Choquette, P.W. and James, N.P. 1987. Diagenesis# 12. Diagenesis in Limestones-3. The deep burial environment. *Geoscience Canada*, **14**, 3-35.

Claire, M.W., Kasting, J.F., Domagal-Goldman, S.D., Stüeken, E.E., Buick, R. and Meadows, V.S., 2014. Modeling the signature of sulfur mass-independent fractionation produced in the Archean atmosphere. *Geochimica et Cosmochimica Acta*, **141**, 365-380.

Crockford, P.W., Kunzmann, M., Bekker, A., Hayles, J., Bao, H., Halverson, G.P., Peng, Y., Bui, T.H., Cox, G.M., Gibson, T.M. and Wörndle, S., 2019. Claypool continued: Extending the isotopic record of sedimentary sulfate. *Chemical Geology*, **513**, 200-225.

Czaja, A.D., Johnson, C.M., Roden, E.E., Beard, B.L., Voegelin, A.R., Nägler, T.F., Beukes, N.J. and Wille, M., 2012. Evidence for free oxygen in the Neoarchean ocean based on coupled iron–molybdenum isotope fractionation. *Geochimica et Cosmochimica Acta*, **86**, 118-137.

Dellwig, O., Leipe, T., März, C., Glockzin, M., Pollehne, F., Schnetger, B., Yakushev, E.V., Böttcher, M.E. and Brumsack, H.J., 2010. A new particulate Mn–Fe–P-shuttle at the redoxcline of anoxic basins. *Geochimica et Cosmochimica Acta*, **74**, 7100-7115.

Duan, Y., Anbar, A.D., Arnold, G.L., Lyons, T.W., Gordon, G.W. and Kendall, B., 2010. Molybdenum isotope evidence for mild environmental oxygenation before the Great Oxidation Event. *Geochimica et Cosmochimica Acta*, **74**, 6655-6668.

Elderfield, H., 1988. The oceanic chemistry of the rare-earth elements. *Philosophical Transactions of the Royal Society of London. Series A, Mathematical and Physical Sciences*, **325**, 105-126.

Eroglu, S., van Zuilen, M.A., Taubald, H., Drost, K., Wille, M., Swanner, E.D., Beukes, N.J. and Schoenberg, R., 2017. Depth-dependent δ13C trends in platform and slope settings of the Campbellrand-Malmani carbonate platform and possible implications for Early Earth oxygenation. *Precambrian Research*, **302**, 122-139.

Fairey, B., Tsikos, H., Corfu, F. and Polteau, S., 2013. U-Pb systematics in carbonates of the Postmasburg Group, Transvaal Supergroup, South Africa: Primary versus metasomatic controls. *Precambrian Research*, **231**, 194-205.

Farquhar, J., Bao, H. and Thiemens, M., 2000. Atmospheric Influence of Earth's Earliest Sulfur Cycle. *Science*, **289**, 756-758.

Frauenstein, F., Veizer, J., Beukes, N., Van Niekerk, H.S. and Coetzee, L.L., 2009. Transvaal Supergroup carbonates: Implications for Paleoproterozoic $\delta^{18}O$ and $\delta^{13}C$ records. *Precambrian Research*, **175**, 149-160.

Garvin, J., Buick, R., Anbar, A.D., Arnold, G.L. and Kaufman, A.J., 2009. Isotopic Evidence for an Aerobic Nitrogen Cycle in the Latest Archean. *Science*, **323**, 1045-1047.

Godfrey, L.V. and Falkowski, P.G. 2009. The cycling and redox state of nitrogen in the Archaean ocean. *Nature Geoscience*, **2**, 725-729.

Gumsley, A.P., Chamberlain, K.R., Bleeker, W., Söderlund, U., de Kock, M.O., Larsson, E.R. and Bekker, A., 2017. Timing and tempo of the Great Oxidation Event. *Proceedings of the National Academy of Sciences*, **114**, 1811-1816.

Guo, Q., Strauss, H., Kaufman, A.J., Schröder, S., Gutzmer, J., Wing, B., Baker, M.A., Bekker, A., Jin, Q., Kim, S.T. and Farquhar, J. 2009. Reconstructing Earth's surface oxidation across the Archean-Proterozoic transition. *Geology*, **37**, 399-402.

Gutzmer, J., & Beukes, N. J. (1996). Mineral paragenesis of the Kalahari managanese field, South Africa. *Ore Geology Reviews*, *11*(6), 405-428

Gutzmer, J. and Beukes, N.J., 1998. High grade manganese ores in the Kalahari manganese field: characterisation and dating of ore forming events, Unpublished Report. Rand Afrikaans University, Johannesburg.

Hood, AvS., Planavsky, N.J., Wallace, M.W. and Wang, X., 2018. The effects of diagenesis on geochemical paleoredox proxies in sedimentary carbonates. *Geochimica et Cosmochimica Acta*, **232**, 265-287.

Izon, G., Zerkle, A.L., Zhelezinskaia, I., Farquhar, J., Newton, R.J., Poulton, S.W., Eigenbrode, J.L. and Claire, M.W., 2015. Multiple oscillations in Neoarchaean atmospheric chemistry. *Earth and Planetary Science Letters*, **431**, 264-273.

Izon, G., Zerkle, A.L., Williford, K.H., Farquhar, J., Poulton, S.W. and Claire, M.W., 2017. Biological regulation of atmospheric chemistry en route to planetary oxygenation. *Proceedings of the National Academy of Sciences*, **114**, E2571-E2579.

Jarvis, K.E., Gray, A.L. and McCurdy, E., 1989. Avoidance of spectral interference on europium in inductively coupled plasma mass spectrometry by sensitive measurement of the doubly charged ion. *Journal of Analytical Atomic Spectrometry*, **4**, 743-747.

Johnson, J.E., Webb, S.M., Thomas, K., Ono, S., Kirschvink, J.L. and Fischer, W.W., 2013. Manganese-oxidising photosynthesis before the rise of cyanobacteria. *Proceedings of the National Academy of Sciences,* **110**, 11238-11243.

Johnson, J.E., Gerpheide, A., Lamb, M.P. and Fischer, W.W., 2014.O_2 constraints from Paleoproterozoic detrital pyrite and uraninite. *Geological Society of America Bulletin*, **126**, 813-830.

Jones, C. and Crowe, S.A. 2013. No evidence for manganese-oxidizing photosynthesis. *Proceedings of the National Academy of Sciences*, **110**, E4118-E4118.

Kamber, B.S., Webb, G.E. and Gallagher, M. 2014. The rare earth element signal in Archaean microbial carbonate: information on ocean redox and biogenicity. *Journal of the Geological Society*, **171**, 745-763.

Kendall, B., Reinhard, C.T., Lyons, T.W., Kaufman, A.J., Poulton, S.W. and Anbar, A.D. 2010. Pervasive oxygenation along late Archaean ocean margins. *Nature Geoscience*, **3**, 647-652.

Kendall, B., van Acken, D. and Creaser, R.A., 2013. Depositional age of the Paleoproterozoic Klipputs member, Nelani Formation (Ghaap Group, Transvaal Supergroup, South Africa) and implications for low-level Re-Os geochronology and Paleoproterozoic global correlations. *Precambrian Research*, **237**, 1-12.

Kent, A.J. and Ungerer, C.A., 2005. Production of barium and light rare earth element oxides during LA-ICP-MS microanalysis. *Journal of Analytical Atomic Spectrometry*, **20**, 1256-1262.

Kurzweil, F., Wille, M., Gantert, N., Beukes, N.J. and Schoenberg, R. 2016. Manganese oxide shuttling in pre-GOE oceans–evidence from molybdenum and iron isotopes. *Earth and Planetary Science Letters*, **452**, 69-78.

Lalonde, S.V. and Konhauser, K.O. 2015. Benthic perspective on Earth's oldest evidence for oxygenic photosynthesis. *Proceedings of the National Academy of Sciences*, **112**, 995-1000.

Lawrence, M.G. and Kamber, B.S. 2006. The behaviour of the rare earth elements during estuarine mixing—revisited. *Marine Chemistry*, **100**, 147-161.

Lawrence, M.G. and Kamber, B.S. 2007. Corrigendum to "The behaviour of the rare earth elements during estuarine mixing—revisited" [Marine Chemistry 100 (2006) 147–161], *Marine Chemistry*, **105,** 181.

Lawrence, M.G., Greig, A., Collerson, K.D. and Kamber, B.S., 2006.Rare earth element and yttrium variability in South East Queensland waterways. *Aquatic Geochemistry*, **12,** 39-72.

Liu, X.M., Hardisty, D.S., Lyons, T.W. and Swart, P.K., 2019. Evaluating the fidelity of the cerium paleoredox tracer during variable carbonate diagenesis on the Great Bahamas Bank. *Geochimica et Cosmochimica Acta*, **248**, 25-42.

Loges, A., Wagner, T., Barth, M., Bau, M., Göb, S. and Markl, G., 2012. Negative Ce anomalies in Mn oxides: the role of Ce4+ mobility during water–mineral interaction. *Geochimica et Cosmochimica Acta*, **86**, 296-317.

Luo, G., Ono, S., Beukes, N.J., Wang, D.T., Xie, S. and Summons, R.E. 2016. Rapid oxygenation of Earth's atmosphere 2.33 billion years ago. *Science Advances*, **2**, p.e1600134.

Miyano, T and Beukes, N.J. 1997. Mineralogy and Petrology of the Contact Metamorphosed Amphibole Asbestos-bearing Penge Iron Formation, Eastern Transvaal, South Africa. *Journal of Petrology*, **38**, 651-676.

Nelson, D.R., Trendall, A.F. and Altermann, W., 1999. Chronological correlations between the Pilbara and Kaapvaal cratons. *Precambrian Research*, **97**, 165-189.

Olson, S.L., Kump, L.R. and Kasting, J.F. 2013. Quantifying the areal extent and dissolved oxygen concentrations of Archean oxygen oases. *Chemical Geology*, **362**, 35-43.

Ostrander, C.M., Nielsen, S.G., Owens, J.D., Kendall, B., Gordon, G.W., Romaniello, S.J. and Anbar, A.D., 2019. Fully oxygenated water columns over continental shelves before the Great Oxidation Event. *Nature Geoscience*, **12**, 186-191.

Philippot, P., Ávila, J.N., Killingsworth, B.A., Tessalina, S., Baton, F., Caquineau, T., Muller, E., Pecoits, E., Cartigny, P., Lalonde, S.V. and Ireland, T.R., 2018. Globally asynchronous sulphur isotope signals require re-definition of the Great Oxidation Event. *Nature Communications*, **9**, 2245.

Pickard, A.L., 2003. SHRIMP U–Pb zircon ages for the Palaeoproterozoic Kuruman Iron Formation, northern Cape Province, South Africa: evidence for simultaneous BIF deposition on Kaapvaal and Pilbara cratons. *Precambrian Research*, **125**, 275-315.

Planavsky, N., Bekker, A., Rouxel, O.J., Kamber, B., Hofmann, A., Knudsen, A. and Lyons, T.W., 2010. Rare earth element and yttrium compositions of Archean and Paleoproterozoic Fe formations revisited: new perspectives on the significance and mechanisms of deposition. *Geochimica et Cosmochimica Acta*, **74**, 6387-6405.

Planavsky, N.J., Asael, D., Hofman, A., Reinhard, C.T., Lalonde, S.V., Knudsen, A., Wang, X., Ossa, F.O., Pecoits, E., Smith, A.J. and Beukes, N.J. 2014. Evidence for oxygenic photosynthesis half a billion years before the Great Oxidation Event. *Nature Geoscience*, **7**, 283-286.

Posth, N.R., Köhler, I., Swanner, E.D., Schröder, C., Wellmann, E., Binder, B., Konhauser, K.O., Neumann, U., Berthold, C., Nowak, M. and Kappler, A., 2013. Simulating Precambrian banded iron formation diagenesis. *Chemical Geology*, **362**, 66-73.

Prokoph, A., Shields, G.A. and Veizer, J., 2008. Compilation and time-series analysis of a marine carbonate δ18O, δ13C, 87Sr/86Sr and δ34S database through Earth history. *Earth-Science Reviews*, **87**, 113-133.

Reinhard, C.T., Planavsky, N.J. and Lyons, T.W., 2013. Long-term sedimentary recycling of rare sulphur isotope anomalies. *Nature*, **497**, 100.

Riding, R., Fralick, P. and Liang, L., 2014. Identification of an Archean marine oxygen oasis. *Precambrian Research*, **251**, 232-237.

Schier, K., Bau, M., Münker, C., Beukes, N. and Viehmann, S., 2018. Trace element and Nd isotope composition of shallow seawater prior to the Great Oxidation Event: Evidence from stromatolitic bioherms in the Paleoproterozoic Rooinekke and Nelani Formations, South Africa. *Precambrian Research*, **315**, 92-102.

Schneiderhan, E.A., Gutzmer, J., Strauss, H., Mezger, K. and Beukes, N.J., 2006.The chemostratigraphy of a Paleoproterozoic MnF-BIF succession – the Voëlwater Subgroup of the Transvaal Supergroup in Griquland West, South Africa. *South African Journal of Geology,* **109,** 63-80**.**

Schröder, S., Bekker, A., Beukes, N.J., Strauss, H. and Van Niekerk, H.S., 2008. Rise in seawater sulphate concentration associated with the Paleoproterozoic positive carbon isotope excursion: evidence from sulphate evaporites in the~ 2.2–2.1 Gyr shallow-marine Lucknow Formation, South Africa. *Terra Nova*, **20**, 108-117.

Schröder, S., Bedorf, D., Beukes, N.J. and Gutzmer, J., 2011. From BIF to red beds: Sedimentology and sequence stratigraphy of the Paleoproterozoic Koegas Subgroup (South Africa). *Sedimentary Geology*, **236**, 25-44.

Scholz, F., McManus, J. and Sommer, S., 2013. The manganese and iron shuttle in a modern euxinic basin and implications for molybdenum cycling at euxinic ocean margins. *Chemical Geology*, **355**, 56-68.

Shields, G. and Veizer, J. 2002. Precambrian marine carbonate isotope database: Version 1.1. *Geochemistry, Geophysics, Geosystems*, **3**, doi:10.1029/2001GC000266.

Takahashi, Y., Sakami, H. and Nomura, M., 2002. Determination of the oxidation state of cerium in rocks by Ce LIII-edge X-ray absorption near-edge structure spectroscopy. *Analytica Chimica Acta*, **468**, 345-354.

Taylor, S.R. and McLennan, S.M. 1985. *The continental crust: its composition and evolution*. Blackwell Scientific Publications, Oxford, pp 312.

Tostevin, R., Shields, G.A., Tarbuck, G.M., He, T., Clarkson, M.O. and Wood, R.A., 2016a. Effective use of cerium anomalies as a redox proxy in carbonate-dominated marine settings. *Chemical Geology*, **438**,146-162.

Tostevin, R., Wood, R.A., Shields, G.A., Poulton, S.W., Guilbaud, R., Bowyer, F., Penny, A.M., He, T., Curtis, A., Hoffmann, K.H. and Clarkson, M.O., 2016b. Low-oxygen waters limited habitable space for early animals. *Nature Communications*, **7**, doi:10.1038/ncomms12818

Tsikos, H. and Moore, J.M. 1997. Petrography and geochemistry of the Paleoproterozoic Hotazel Iron-Formation, Kalahari manganese field, South Africa; implications for Precambrian manganese metallogenesis. *Economic Geology*, **92**, 87-97.

Tsikos, H., Beukes, N.J., Moore, J.M. and Harris, C. 2003. Deposition, diagenesis, and secondary enrichment of metals in the Paleoproterozoic Hotazel iron formation, Kalahari Manganese Field, South Africa. *Economic Geology*, **98**, 1449-1462.

Veizer, J., Clayton, R.N. and Hinton, R.W., 1992. Geochemistry of Precambrian carbonates: IV. Early Paleoproterozoic (2.25±0.25 Ga) seawater. *Geochimica et Cosmochimica Acta,* 56, 875-885.

Voegelin, A.R., Nägler, T.F., Beukes, N.J. and Lacassie, J.P., 2010. Molybdenum isotopes in late Archaean carbonate rocks: Implications for Early Earth oxygenation. *Precambrian Research*, **182**, 70-82.

Voigt, M., Mavromatis, V. and Oelkers, E.H., 2017. The experimental determination of REE partition coefficients in the water-calcite system. *Chemical Geology*, **462**, 30-43.

Warke, M.R. and Schröder, S., 2018. Synsedimentary fault control on the deposition of the Duitschland Formation (South Africa): Implications for depositional settings, Paleoproterozoic stratigraphic correlations, and the GOE. *Precambrian Research*, **310**, 348-364.

Warke, M.R., Schröder, S. and Strauss, H., 2018. Testing models of pre-GOE environmental oxidation: A Paleoproterozoic marine signal in platform dolomites of the Tongwane Formation (South Africa). *Precambrian Research*, **313**, 205-220.

Warke, M.R., Edwards, N.P., Wogelius, R.A., Manning, P.L., Bergmann, U., Egerton, V.M., Kimball, K.C., Garwood, R.J., Beukes, N.J. and Schröder, S., 2019. Decimeter-scale mapping of carbonate-controlled trace element distribution in Neoarchean cuspate stromatolites. *Geochimica et Cosmochimica Acta*, **261**, 56-75.

Wille, M., Kramers, J.D., Nägler, T.F., Beukes, N.J., Schröder, S., Meisel, T., Lacassie, J.P. and Voegelin, A.R., 2007. Evidence for a gradual rise of oxygen between 2.6 and 2.5 Ga from Mo isotopes and Re-PGE signatures in shales. *Geochimica et Cosmochimica Acta*, **71**, 2417-2435.

Zerkle, A.L., Claire, M.W., Domagal-Goldman, S.D., Farquhar, J. and Poulton, S.W., 2012. A bistable organic-rich atmosphere on the Neoarchaean Earth. *Nature Geoscience*, **5**, 359-363

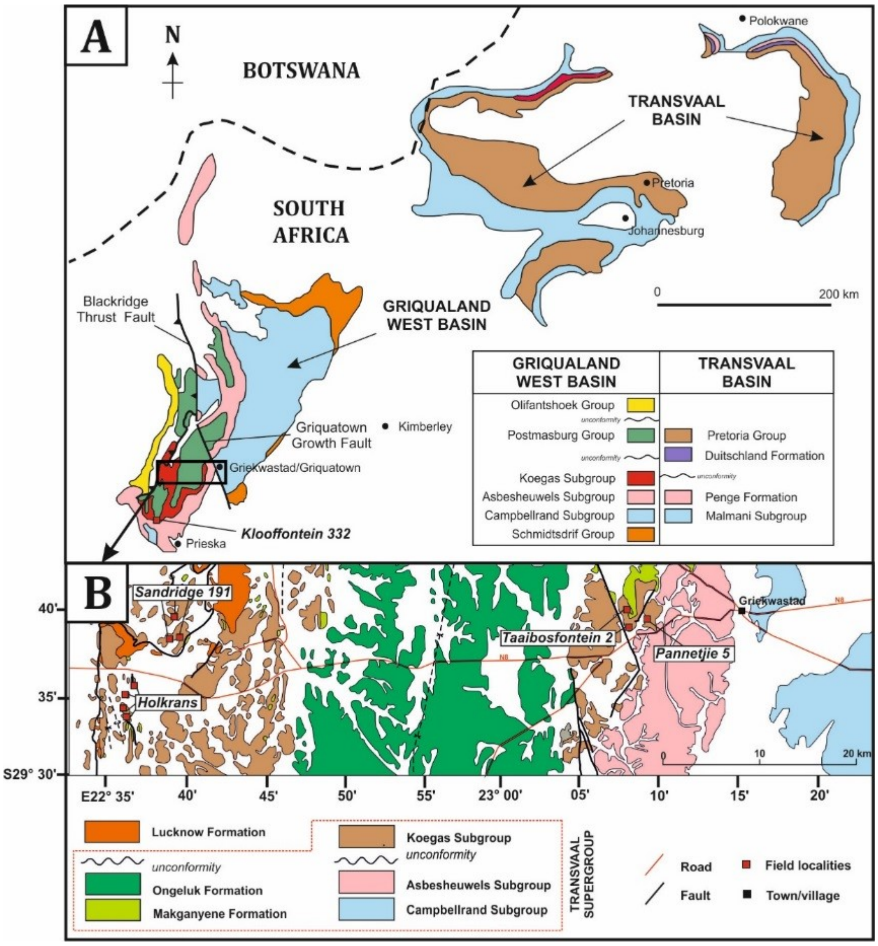

Figure 1: (A) regional map of the Transvaal Supergroup in South Africa where the black rectangle in the southern half of the Griqualand West Basin shows a localised map (B) of the study area west of Griquatown in the Northern Cape Province, South Africa. Localities visited are shown in panel B, including the position of the farms of Taaibosfontein and Sandridge.

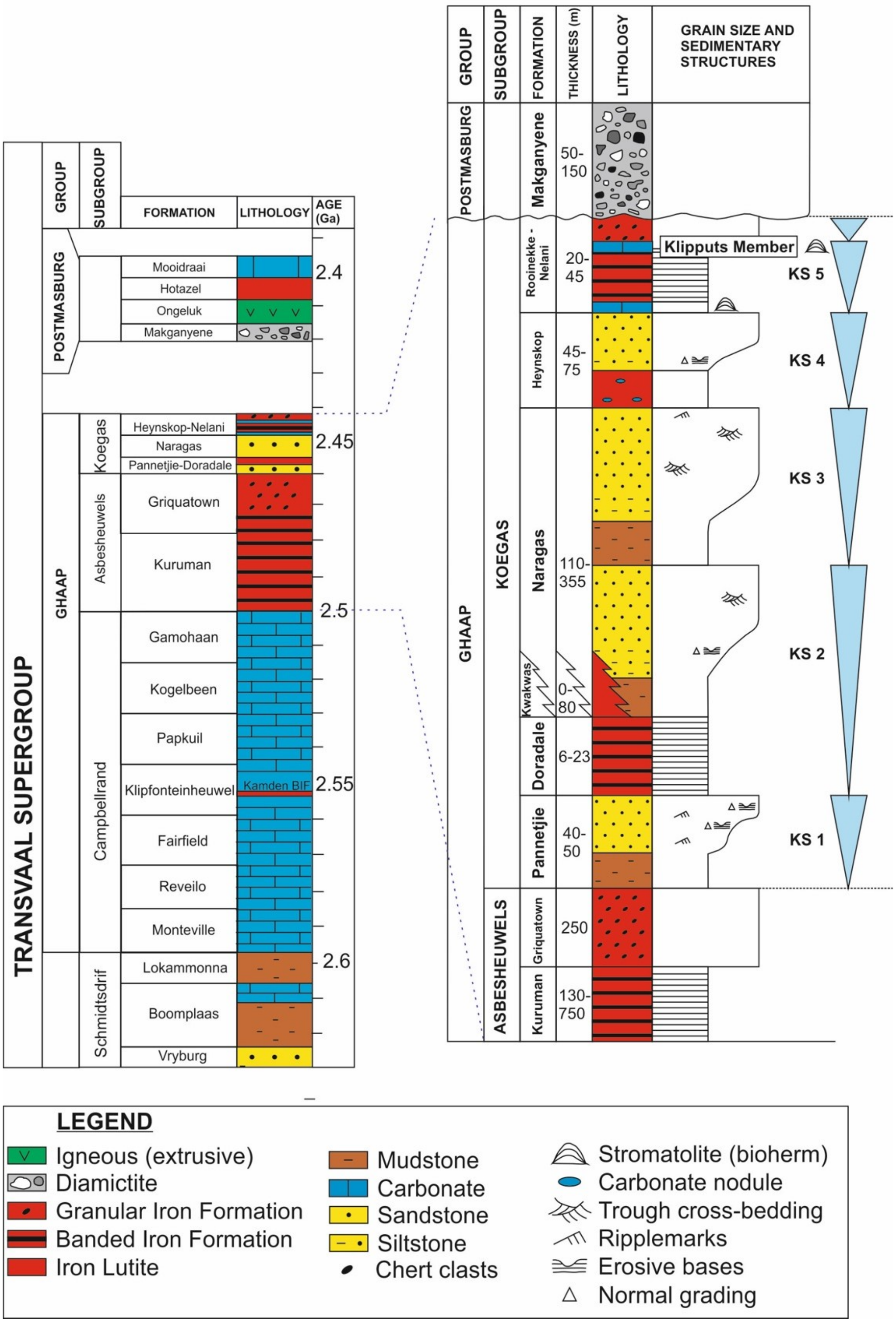

Figure 2: overview stratigraphic column of the Transvaal Supergroup in the Griqualand West Basin (left) with magnified stratigraphic profile through the Koegas Subgroup (right). Blue triangles in the Koegas stratigraphic profiles indicate coarsening-upward, regressive depositional sequences after Schröder et al. (2011). Absolute and relative ages used for constraint are discussed in the text.

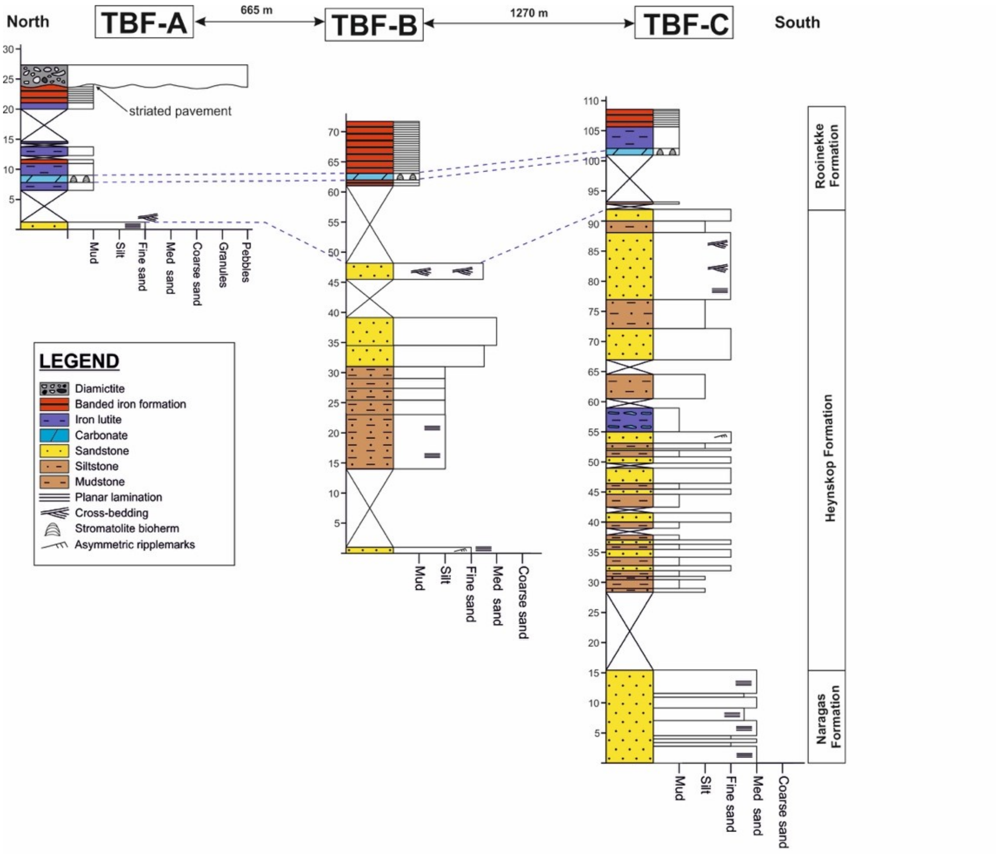

Figure 3: sedimentological profiles through the upper Koegas Subgroup and lower Postmasburg measured on the farm Taaibosfontein.

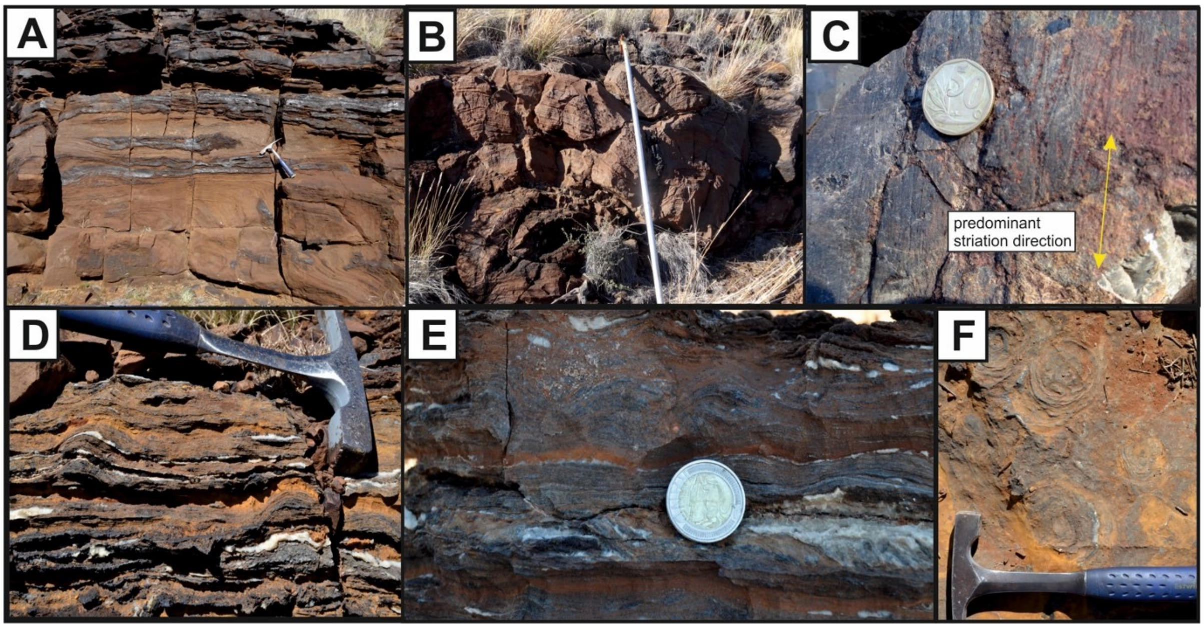

Figure 4: field images showing: stromatolitic bioherms on the farm Taaibosfontein exposed (A) in log TBF-B and (B) in the marker bed between logs TBF-B and TBF-C; (C) striated bedrock is visible beneath the Makganyene diamictite in log TBF-A; (D-F) small domal stromatolites preserve in crinkly-laminated carbonates of the Klipputs Member on the farm Sandridge.

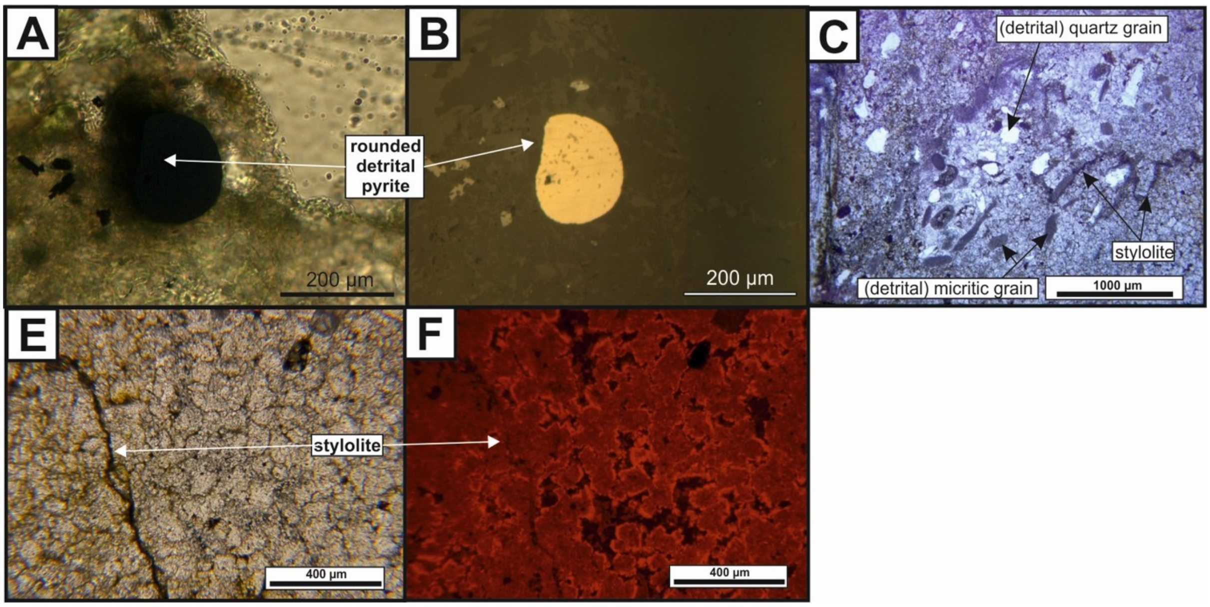

Figure 5: thin section images of Taaibosfontein units showing: transmitted (A) and reflected (B) light images of rounded detrital pyrite within deltaic litharenites; (C) angular and sub-angular detrital quartz and lithic clasts concentrated along dissolution surfaces in Taaibosfontein carbonates; and transmitted (E) and cathodoluminescence (F) images monotonous, recrystallized Taaibosfontein planar-s ferroan dolostone with brightly luminescent rims on areas with a planar-e fabric.

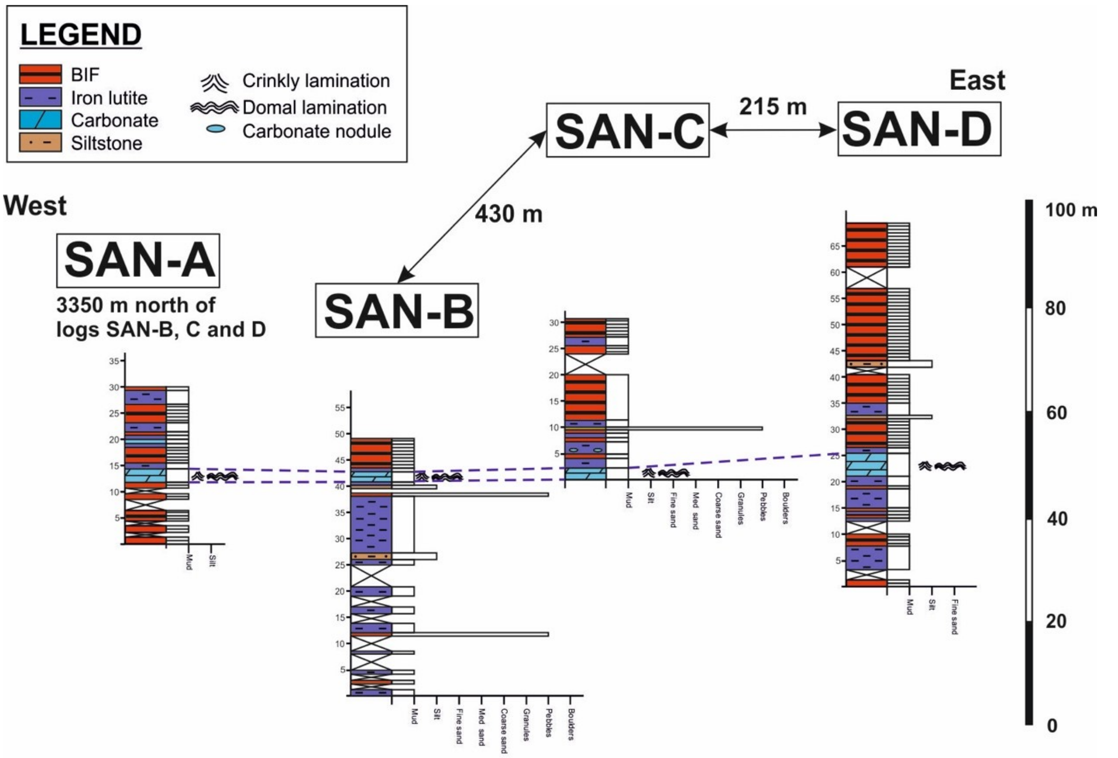

Figure 6: sedimentological profiles through the upper Koegas Subgroup on the farm Sandridge. Measured logs intersect carbonates of the Klipputs Member at the base of the Nelani Formation.

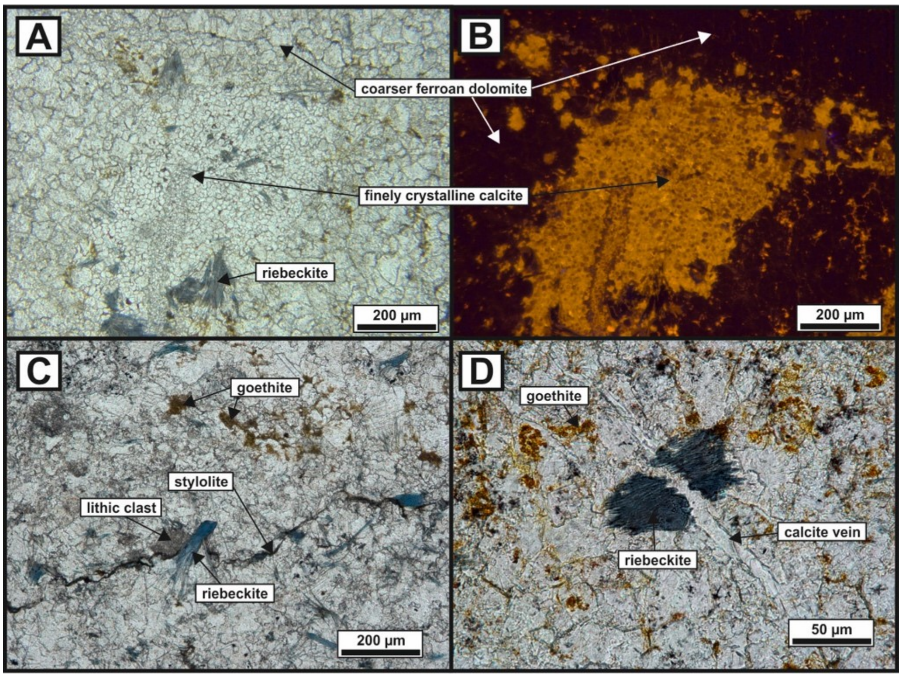

Figure 7: thin section images of Sandridge carbonates showing: (A-B) textural and luminescience difference between pockets of finer ferroan calcite and coarser ferroan dolomite with minor riebeckite and goethite; (C) stylolite overprinting riebeckite; (D) calcite veins which cross-cut riebeckite.

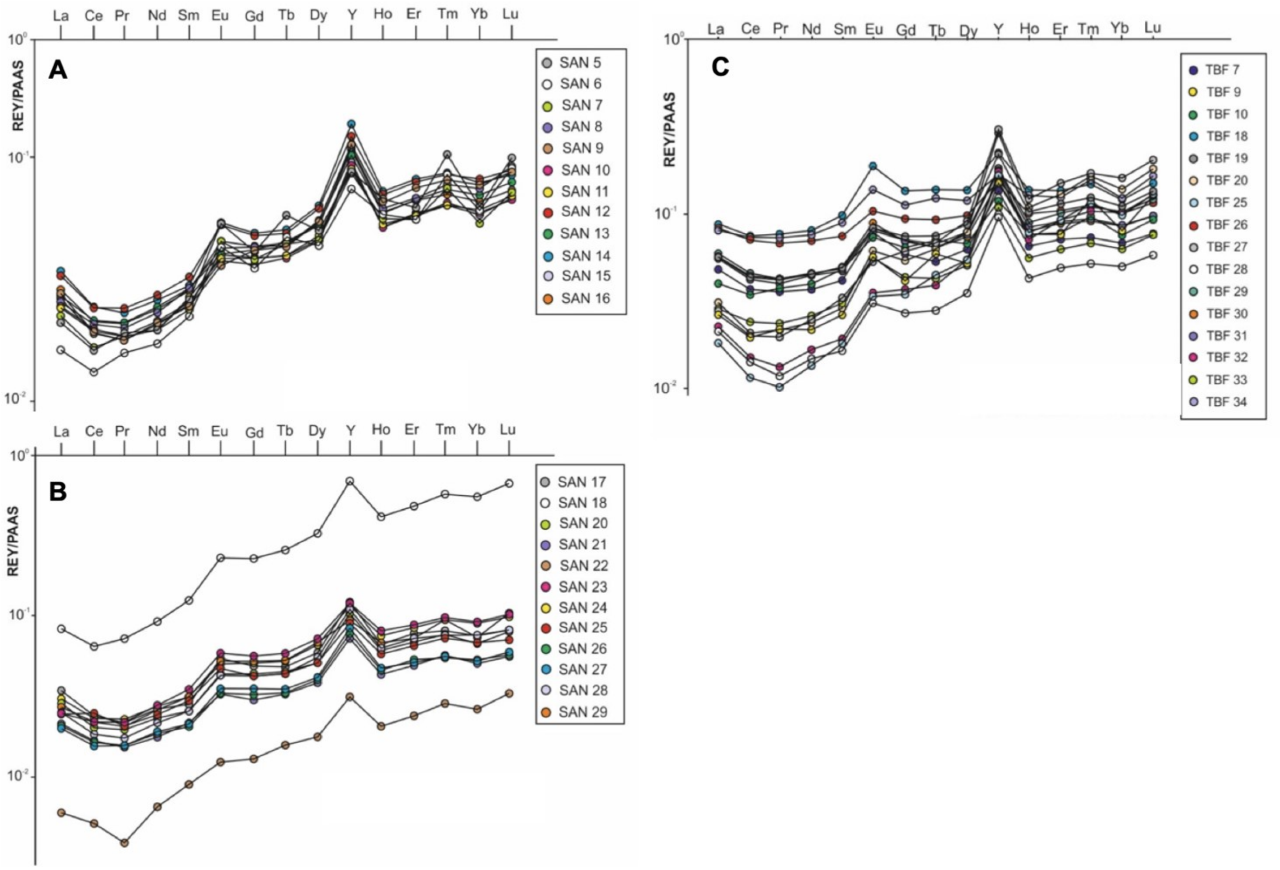

Figure 8: PAAS normalised rare earth element and yttrium (REY_{SN}) arrays for stromatolitic carbonates from the localities of Sandridge (A, B) and Taaibosfontein (C). Carbonates from these localities show marine characteristics: positive La_{SN} and Gd_{SN} anomalies, higher relative heavy REE concentrations and elevated Y/Ho anomalies, in addition to small positive Eu_{SN} anomalies.

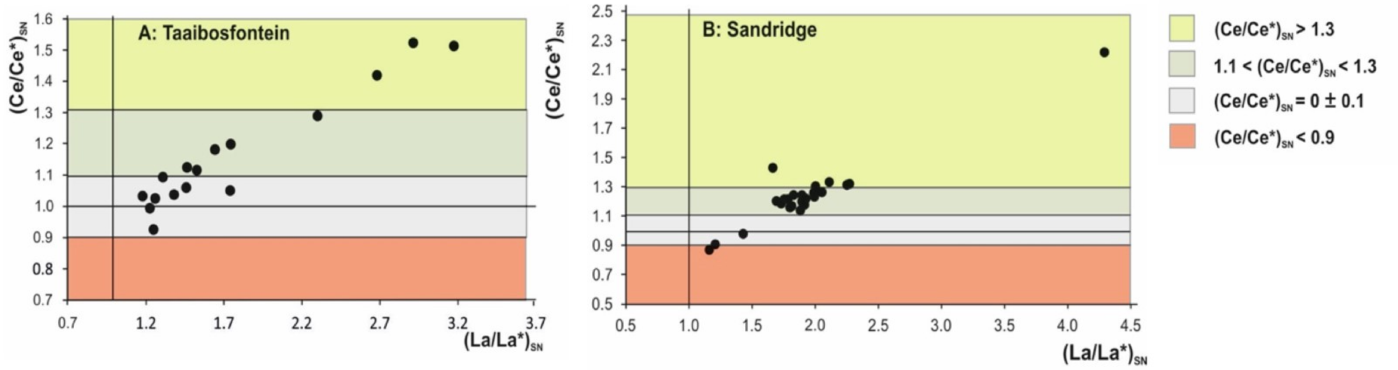

Figure 9: calculated cerium and lanthanum anomalies for samples from the farms (A) Taaibosfontein and (B) Sandridge. The two green shaded areas correspond to positive cerium anomalies, grey shaded areas indicate no significant anomaly, and red shaded areas indicate negative cerium anomalies.

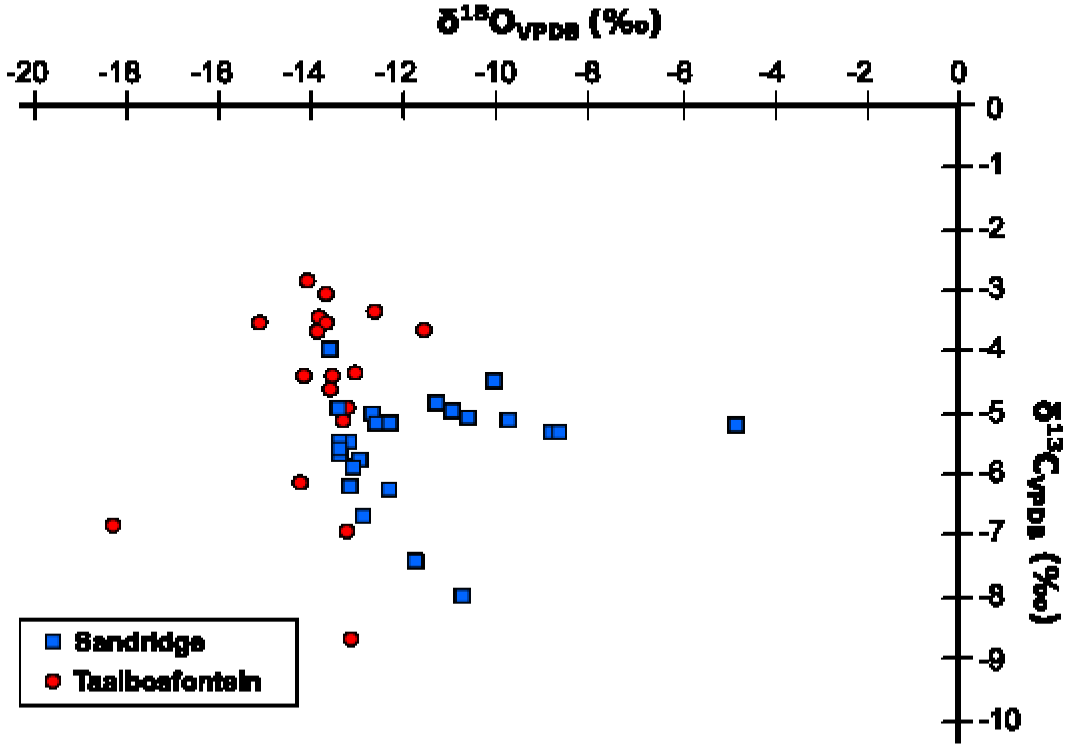

Figure 10: $\delta^{13}C_{carb}$ and $\delta^{18}O_{carb}$ values (‰$_{VPDB}$) for samples from the localities of Taaibosfontein (red circles) and Sandridge (blue squares). Error bars on each measurement are incorporated within the size of the symbol.

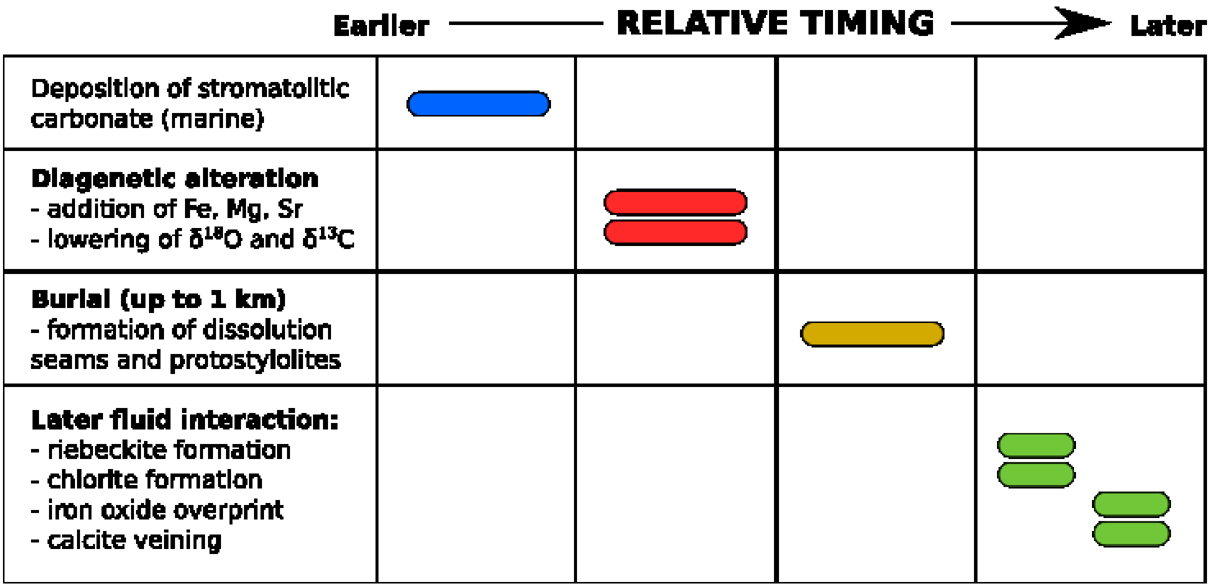

Figure 11: summary of the paragenetic evolution of upper Koegas carbonates from the localities of Taaibosfontein and Sandridge. It is only possible to constrain the relative timing of events which are determined by cross-cutting relations and spatial associations (see text and figures for further discussion).

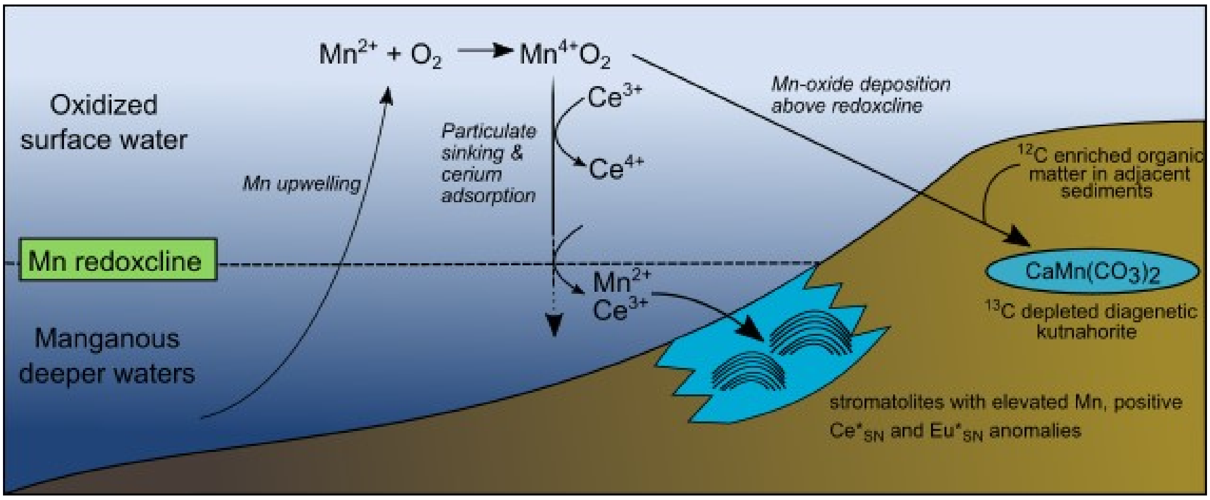

Figure 12: schematic diagram illustrating processes by which positive Ce_{SN} anomalies are generated and preserved in the Koegas Basin. In upper surface waters free oxygen produced through oxygenic photosynthesis facilitates the oxidation of upwelling Mn2+ forming particulate Mn4+ oxides. Cerium oxidation is facilitated on the surface of these particulates, shuttling Ce from the upper portion of the water column. At a redoxcline sinking oxidised particulates are reduced, releasing Mn^{2+} and Ce^{3+} which can be incorporated into carbonates at this depth (Tostevin et al., 2016b). A similar Mn-redox shuttling mechanism has been proposed in the Koegas basin to explain $\delta^{56}Fe$ and $\delta^{98}Mo$ trends (Kurzweil et al., 2016). Oxidised Mn-particulates that are deposited above the Mn-redoxcline could then have been reduced by ^{12}C rich fluids during diagenesis to form kutnahorite horizons.